

## NUCLEAR DEFORMATION AND DOUBLE FINE STRUCTURE IN THE BINARY COLD FISSION

D. S. DELION<sup>1</sup>, A. SANDULESCU<sup>2</sup>

<sup>1</sup> *National Institute of Physics and Nuclear Engineering,  
Bucharest-Măgurele, POB MG-6, Romania*

<sup>2</sup> *Center for Advanced Studies in Physics, Romanian Academy  
Calea Victoriei 125, Bucharest, Romania*

(Received October 26, 2005)

*Abstract.* We investigate the important role played by the nuclear deformations on low-lying rotational yields in the cold fission of  $^{252}\text{Cf}$ . A fissioning state is considered as a resonance in the potential well between the emitted fragments. The interaction is given by a double folding procedure using M3Y plus Coulomb forces. The only free parameter is the strength of a repulsive potential, adjusting the position of a resonant state to the experimental  $Q$ -value. We generalize our previous approach by using a common rotational basis and considering all degrees of freedom. As fissioning states we select those resonances which are oriented close to the pole-to-pole configuration in the overlapping region. We predict a strong dependence of decay yields upon the quadrupole and hexadecapole deformation parameters. Predictions of rotational yields for ten possible cold splittings of  $^{252}\text{Cf}$  are given.

PACS: 21.60.Gx, 24.10.Eq, 25.85.Ca

*Key words:* nuclear deformation, cold fission, resonant state, fine structure.

### 1. INTRODUCTION

In the last years an intense experimental activity was performed in order to investigate cold (neutron-less) binary and ternary fission process of  $^{252}\text{Cf}$  [1, 2, 3, 4, 5, 6, 7, 8, 9]. It involved modern facilities, as the Gammasphere and Eurogam, which were able to identify this rare process using the triple  $\gamma$ -rays coincidence technique.

The measurements confirmed the idea that this process is a natural extension of the cluster radioactivity [10, 11]. A very convincing theoretical evidence that it has a sub-barrier character was the WKB penetration calculation, using a double folding potential with M3Y plus Coulomb nucleon-nucleon forces. This simple estimate was able to reproduce the gross features of the binary cold fragmentation isotopic yields of  $^{252}\text{Cf}$  [12].

The yields of rotational states were extracted from the intensities of  $\gamma$ -rays emitted in coincidence during the deexcitation of fragments for  $^{104}\text{Mo}$ - $^{148}\text{Ba}$  and

$^{106}\text{Mo}$ - $^{146}\text{Ba}$  [2]. It was shown that the cold fission population is centered around the low-lying  $2^+$  and  $4^+$  states and the states higher than  $6^+$  are practically not populated. This proves the assumption concerning the cold rearrangement of nucleons during the cold fission.

The role of Coulomb excitations under various assumptions of the initial spin distribution at the scission point was studied in Ref. [13] within a semiclassical time dependent formalism. Here only the quadrupole-quadrupole Coulomb term was considered.

In two recent papers [14, 15] we analyzed the double fine structure of emitted fragments within the stationary scattering formalism. The fissioning state was identified with a resonance in the inter-fragment potential, calculated using the double folding procedure. For the external part of the potential we used the two-body M3Y plus Coulomb interaction. The energy was adjusted to reproduce the experimental  $Q$ -value by an internal repulsive core.

Concerning the basis we made some simplifications. We combined two bases, namely rotational functions for the external region matched with planar vibrational functions describing the internal motion. Thus, we neglected the torsional degrees of freedom.

The aim of this paper is to simplify this approach by using a common rotational basis, as in our recent Ref. [16]. This will allow us to take into account all degrees of freedom, generalizing our previous approach. Moreover, we will show that the internal “oscillatory” character around the pole-to-pole configuration of wave functions is automatically achieved, without any special hypothesis. In this way the proposed method becomes suitable not only for fission, but also to describe capture processes in the most general framework.

The paper is organized according to the following plan. In Section 2 we describe the cold fission process as a decay of a stationary resonant state, using a common rotational basis for both internal (overlapping) and external regions. The yields of rotational states are estimated as the decay widths within the coupled channel formalism. In Section 3 we apply this formalism to analyze several splittings of  $^{252}\text{Cf}$ . We put in evidence the crucial role of deformation parameters on the yields of rotational states. In the last Section we draw the conclusions.

## 2. THEORETICAL BACKGROUND

We describe the fission process as in Ref. [15], using the stationary Schrödinger equation

$$H\Psi(\mathbf{R}, \Omega_1, \Omega_2) = E\Psi(\mathbf{R}, \Omega_1, \Omega_2), \quad (2.1)$$

where  $\mathbf{R} = (R, \Omega)$  denotes the distance between the centers of two deformed

nuclei. The orientation of their major axes in the laboratory system is given by Euler angles  $\Omega_k = (\varphi_k, \theta_k, 0)$ ,  $k = 1, 2$ .

The most favourable fissioning configuration is the pole-to-pole ( $p$ - $p$ ) one, with  $\Omega_1 = \Omega_2 = \Omega$ , where the Coulomb barrier has the lowest possible value. Before the scission point the potential rapidly increases around this configuration in the direction of angular variables [17]. By approaching the scission point the potential becomes gradually flatter, and for large distances, where the fragments are separated, the interaction is given only by the Coulomb potential. In this region the two nuclei are left in excited rotational states.

The Hamiltonian can be written as follows

$$H = -\frac{\hbar^2}{2\mu} \nabla_R^2 + H_1(\Omega_1) + H_2(\Omega_2) + V(\mathbf{R}, \Omega_1, \Omega_2), \quad (2.2)$$

where  $\mu$  is the reduced mass of the dinuclear system and  $H_k$  are the Hamiltonians describing the rotation of the fragments. We estimate the interaction between nuclei in terms of the double folding between the nuclear densities [18] by using the M3Y nucleon-nucleon [19] plus Coulomb force. This potential can be divided into a spherical and a deformed component

$$V(\mathbf{R}, \Omega_1, \Omega_2) = V_0(R) + V_D(\mathbf{R}, \Omega_1, \Omega_2). \quad (2.3)$$

By expanding the nuclear densities in multipoles one obtains the deformed part of the interaction as follows

$$V_D(\mathbf{R}, \Omega_1, \Omega_2) = \sum_{\lambda_0 \lambda_1 \lambda_2} V_{\lambda_0 \lambda_1 \lambda_2}(R) \mathcal{Y}_{\lambda_0 \lambda_1 \lambda_2}(\Omega, \Omega_1, \Omega_2), \quad (2.4)$$

where the term  $(\lambda_0 \lambda_1 \lambda_2) = (000)$  is excluded from summation. Here the angular part of the wave function has the following ansatz

$$\mathcal{Y}_{\lambda_0 \lambda_1 \lambda_2}(\Omega, \Omega_1, \Omega_2) = \left\{ Y_{\lambda_0}(\Omega) \otimes \left[ Y_{\lambda_1}(\Omega_1) \otimes Y_{\lambda_2}(\Omega_2) \right]_{\lambda_0} \right\}_0. \quad (2.5)$$

If the rotational states of fragments belong to the ground band the wave function is given by a similar superposition, *i.e.*,

$$\Psi(\mathbf{R}, \Omega_1, \Omega_2) = \frac{1}{R} \sum_{II_1 I_2} f_{II_1 I_2}(R) \mathcal{Y}_{II_1 I_2}(\Omega, \Omega_1, \Omega_2). \quad (2.6)$$

It is interesting to derive the expression of the angular function in the so-called ‘‘molecular’’ intrinsic system of coordinates, defined by the Euler angle  $\Omega$  as follows

$$\Omega'_k = \Omega^{-1} \Omega_k, \quad k = 1, 2. \quad (2.7)$$

One obtains

$$\mathcal{Y}_{I_1 I_2}(\Omega, \Omega'_1, \Omega'_2) = \frac{(-)^l}{\sqrt{4\pi}} \left[ Y_{I_1}(\Omega'_1) \otimes Y_{I_2}(\Omega'_2) \right]_{l0}. \quad (2.8)$$

This expression can also be obtained by replacing  $\Omega = 0$  in Eq. (2.5). Thus, the interaction (2.4), as well as the wave function (2.6) does not depend on the whole orientation of the system in space, given by  $\Omega$ .

By using the orthonormality of angular functions entering superposition (2.6) one obtains in a standard way the coupled system of differential equations for radial components

$$\frac{d^2 f_{I_1 I_2}(R)}{d\rho_{12}^2} = \sum_{I' I'_2} A_{I_1 I_2; I' I'_2}(R) f_{I' I'_2}(R), \quad (2.9)$$

where the coupling matrix is given by

$$A_{I_1 I_2; I' I'_2}(R) = \left[ \frac{l(l+1)}{\rho_{12}^2} + \frac{V_0(R)}{E_{12}} - 1 \right] \delta_{I' I'_2} \delta_{I_1 I'_1} \delta_{I_2 I'_2} + \frac{1}{E_{12}} \langle \mathcal{Y}_{I_1 I_2} | V_D(R) | \mathcal{Y}_{I' I'_2} \rangle. \quad (2.10)$$

Here we introduced the following short-hand notations

$$\begin{aligned} \rho_{12} &= \kappa_{12} R, & \kappa_{12} &= \sqrt{\frac{2\mu E_{12}}{\hbar^2}}, \\ E_{12} &= E - E_{I_1} - E_{I_2}, \end{aligned} \quad (2.11)$$

where  $E_{I_1}$ ,  $E_{I_2}$  are the ground band energies of the emitted fragments. The matrix element entering Eq. (2.10) is given by

$$\begin{aligned} \langle \mathcal{Y}_{I_1 I_2} | V_D(R) | \mathcal{Y}_{I' I'_2} \rangle &= \sum_{\lambda_0 \lambda_1 \lambda_2} V_{\lambda_0 \lambda_1 \lambda_2}(R) (-)^{\lambda_1 + \lambda_2 - \lambda_0 + l} \frac{\hat{I}'_1 \hat{I}'_2 \hat{I}' \hat{\lambda}_1 \hat{\lambda}_2}{(4\pi)^{3/2}} \times \\ &\times \langle l, 0; I', 0 | \lambda_0, 0 \rangle \langle I'_1, 0; \lambda_1, 0 | I_1, 0 \rangle \langle I'_2, 0; \lambda_2, 0 | I_2, 0 \rangle \left\{ \begin{matrix} I_1 & I_2 & l \\ I'_1 & I'_2 & I' \\ \lambda_1 & \lambda_2 & \lambda_0 \end{matrix} \right\}, \end{aligned} \quad (2.12)$$

where the bracket denotes Clebsch-Gordan recoupling coefficient, curly bracket 9-j symbol and  $\hat{I} = \sqrt{2I+1}$ .

We will shortly remind the procedure to integrate numerically this system of equations and to find resonant states. Let us introduce the short-hand index

$$(I_1 I_2) \rightarrow I. \quad (2.13)$$

We first define  $N$  independent vector functions, satisfying inside the repulsive core at  $R = R_0$  the following boundary conditions

$$\mathcal{R}_{lk}(R_0) = \delta_{lk}\varepsilon, \quad (2.14)$$

where  $\varepsilon$  is an arbitrary small number. We then determine  $N$  independent outgoing Coulomb functions, *i.e.*

$$\mathcal{H}_{lk}^{(+)}(R) = \mathcal{G}_{lk}(R) + i\mathcal{F}_{lk}(R) \xrightarrow{R \rightarrow \infty} \delta_{lk}H_l^{(+)}(\kappa_l R) \equiv \delta_{lk} [G_l(\kappa_l R) + iF_l(\kappa_l R)], \quad (2.15)$$

where  $G_l(\kappa_l R)$ ,  $F_l(\kappa_l R)$  are the irregular and regular spherical Coulomb wave functions, respectively, depending on the momentum  $\kappa_l$  in the channel  $l$ . Each component of the solution is built as a superposition of these  $N$  independent fundamental solutions. We impose the matching boundary decay conditions at the radius  $R_1$  inside the barrier, *i.e.* to have outgoing waves in all channels

$$f_i(R_1) = \sum_k \mathcal{R}_{lk}(R_1)C_k = \sum_k \mathcal{H}_{lk}^{(+)}(R_1)S_k, \quad (2.16)$$

and a similar condition for derivatives. This gives the following secular equation

$$\det \begin{bmatrix} \mathcal{R}(R_1) & \mathcal{H}^{(+)}(R_1) \\ d\mathcal{R}(R_1)/dR & d\mathcal{H}^{(+)}(R_1)/dR \end{bmatrix} \approx \det \begin{bmatrix} \mathcal{R}(R_1) & \mathcal{G}(R_1) \\ d\mathcal{R}(R_1)/dR & d\mathcal{G}(R_1)/dR \end{bmatrix} = 0. \quad (2.17)$$

The first condition is exact and it is fulfilled for complex energies, determining the resonant states. In our case they practically coincide with the real scattering resonant states, because the imaginary parts of energies are much smaller than the corresponding real parts. This corresponds to vanishing regular Coulomb functions  $F_l$  inside the barrier. Therefore the above approximation given by the second equality is very good. The roots of the system (2.17) do not depend upon the matching radius  $R_1$ .

The coefficients  $C_k$ ,  $S_k$  are fully determined from the normalisation of the internal wave function

$$\sum_{ll_2} \int_{R_0}^{R_2} |f_{ll_2}(R)|^2 dR = 1, \quad (2.18)$$

where  $R_2$  is the external turning point. We used here again the complete notation for the basis.

The total decay width is a sum over partial channel widths. It can be derived from the continuity equation in a straightforward way as follows

$$\Gamma = \sum_{ll_2} \Gamma_{ll_2} = \sum_l \hbar v_{ll_2} \lim_{R \rightarrow \infty} |f_{ll_2}(R)|^2 = \sum_{ll_2} \hbar v_{ll_2} |S_{ll_2}|^2, \quad (2.19)$$

where  $v_{ll_1l_2}$  is the center of mass velocity at infinity in the channel  $(l, I_1, I_2)$ , *i.e.*

$$v_{ll_1l_2} = \frac{\hbar\kappa_{l_2}}{\mu}. \quad (2.20)$$

### 3. NUMERICAL APPLICATION

We selected among the binary splittings of  $^{252}\text{Cf}$  the most intense even-even events, given in Table 1. We analyzed only the cold fission process, *i.e.* we supposed ground-state (gs) deformations in the final fragments. The emitted fragments are neutron rich unstable nuclei. Therefore the ground state deformations are given by a suitable systematics. In columns 6–9 we give quadrupole, as well as hexadecapole deformations for both fragments, according to Ref. [20]. We mention here that in Ref. [12] it was clearly evidenced the important role played by hexadecapole deformations on the penetration process.

In expanding the double-folding interaction (2.4) and the wave function (2.6) we used the same rotational basis  $(l, I_1, I_2)$ , given in Table 2. We considered axially deformed fragments and therefore only even relative  $l$  and fragment angular momenta  $I_1I_2 = 0, 2, 4$ . Thus, we supposed that the states starting from  $J = 6^+$  are practically not feeded, in agreement with the experimental situation.

Table 1

The charge and mass numbers for ten different splittings of  $^{252}\text{Cf}$ . The quadrupole and hexadecapole deformations of the two fragments are given in columns 6–9. In the last two columns are given the logarithms of the total decay widths by using one and 15 states in the basis, respectively. We considered the first resonant states. By stars are given the decay widths of second resonant states.

No.	$Z_1$	$A_1$	$Z_2$	$A_2$	$b_2^{(1)}$	$b_4^{(1)}$	$b_2^{(2)}$	$b_4^{(2)}$	$Q$ [MeV]	$\lg(\Gamma_1)$	$\lg(\Gamma_{15})$
1	38	98	60	154	0.357	0.056	0.270	0.114	208.90	-1.094	-1.175
2	38	100	60	152	0.368	0.033	0.262	0.128	206.41	-2.679	-0.246
2*											-1.692
3	40	100	58	152	0.358	0.039	0.261	0.111	212.42	-1.803	-1.515
4	40	102	58	150	0.369	0.017	0.252	0.126	212.76	-1.497	-0.369
4*											-0.780
5	40	104	58	148	0.381	0.005	0.216	0.109	213.35	-2.322	-2.542
6	42	104	56	148	0.349	0.030	0.236	0.131	214.67	-2.778	-1.020
7	42	106	56	146	0.361	0.002	0.199	0.100	217.38	-2.282	-1.164
8	42	108	56	144	0.333	0.027	0.164	0.078	219.15	-2.403	-2.384
9	44	110	54	142	0.250	0.044	0.145	0.075	220.94	-5.735	-4.852
9*											-3.987
10	44	112	54	140	0.258	0.064	0.116	0.070	224.37	-3.606	-2.481

Table 2

The rotational basis  $(l, I_1, I_2)$ 

No.	$l$	$I_1$	$I_2$
1	0	0	0
2	0	2	2
3	0	4	4
4	2	2	0
5	2	0	2
6	2	2	2
7	2	4	4
8	2	4	2
9	2	2	4
10	4	4	0
11	4	0	4
12	4	2	2
13	4	4	4
14	4	4	2
15	4	2	4

In Fig. 1 we plotted by a solid line the pole-to-pole radial component of the potential, defined as

$$V_{p-p}(R) = V(R, \Omega, \Omega, \Omega), \quad (3.1)$$

for the splitting 6 in Table 1, *i.e.*  $^{104}\text{Mo}+^{148}\text{Ba}$ . From Eq. (2.8) it becomes clear that indeed this interaction does not depend upon Euler angles. This potential gives a much lower Coulomb barrier in comparison with the pure spherical component  $V_0(R)$ , plotted by a dashed line. Therefore in our calculation we considered as a spherical component the pole-to-pole interaction  $V_{p-p}(R)$  until the intersection with the true spherical part  $V_0(R)$ . Beyond this point, which is close to the touching configuration,  $V_0(R)$  becomes energetically more favourable and the two fragments start to rotate separately.

The potential in Fig. 1 corresponds to a repulsive part reproducing the experimental  $Q$ -value, given in the column 10 of the Table 1, as the energy of the lowest resonant state. The 15 radial components of the wave function  $f_l(R)$ ,  $l \rightarrow (l, I_1, I_2)$  are plotted in Fig. 2. They are mainly concentrated in the pocked-like internal part of the potential in Fig. 1 and the largest components have zero nodes.

First of all we estimated total decay widths, using Eq. (2.19). In Ref. [12] they are called total yields. The results are given by the last column of the Table 1. We compared these values with the results obtained using only the first component

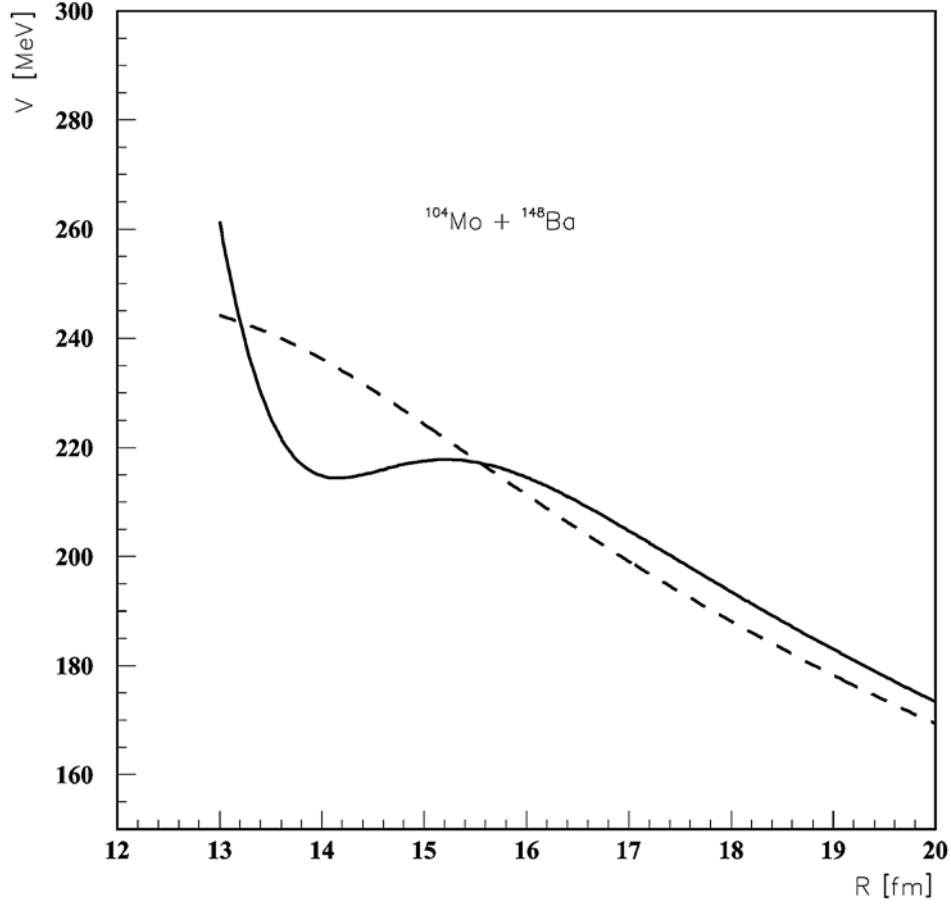


Fig. 1 – The double folding potential  $V_{p-p}(R)$  for the pole-to-pole configuration defined by Eq. (3.1) (solid line) and the spherical component  $V_0(R)$  in Eq. (2.3) (dot-dashed line) for the splitting  $^{104}\text{Mo}+^{148}\text{Ba}$ .

of the Table 2, *i.e.*, the penetration through a spherical barrier. These values are given in the column 11. As a rule they are lower up to one order of magnitude in comparison with the full-basis calculation. Exceptions are the lines 2 and 4.

In order to understand this feature we computed the angular distribution of the wave function (2.6) for a radius corresponding to maximal values in Fig. 2, *i.e.*, in to the minimum of the pocket-like potential. We plotted in Fig. 3 by dashed lines the angular probability depending upon the angle  $\theta_1$  for various values of  $\theta_2 = 0^\circ, 30^\circ, 60^\circ, 90^\circ$  and  $\varphi_1 = \varphi_2 = 0$ . Here we considered all angles in the “molecular” intrinsic system of coordinates defined by Eq. (2.7), *i.e.*,

$$\Omega'_k = (\varphi_k, \theta_k, 0), \quad k = 1, 2. \quad (3.2)$$

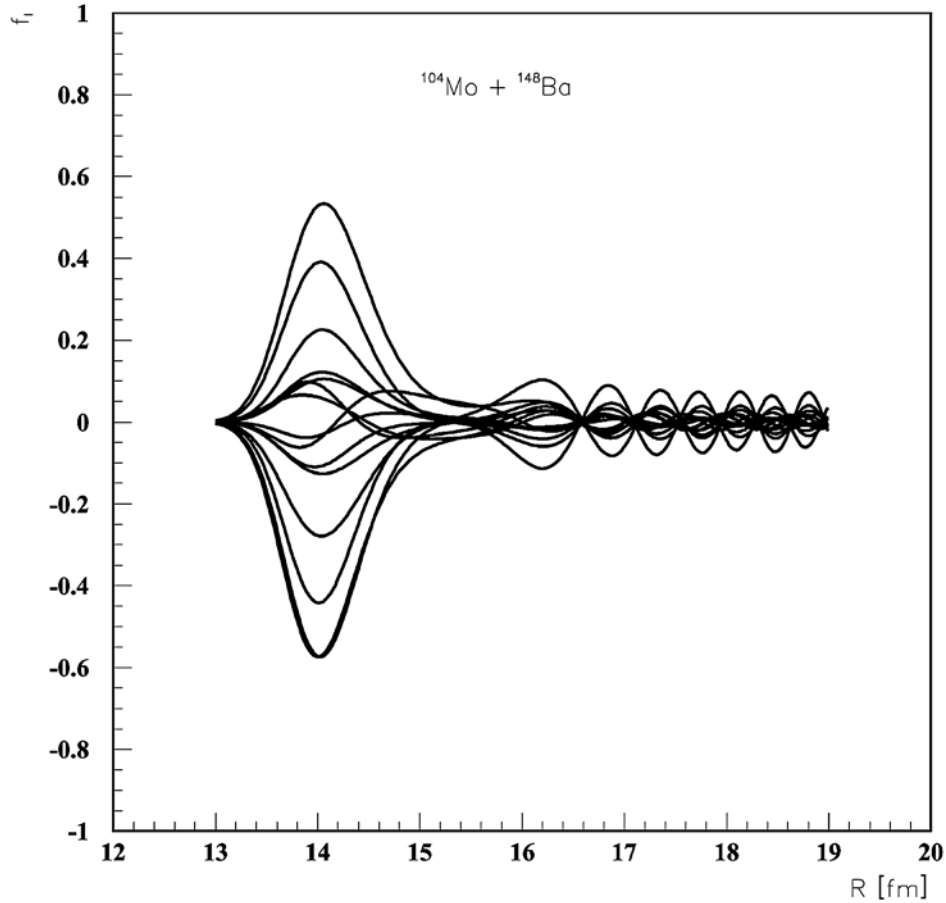


Fig. 2 – The radial components of the wave function defined by Eq. (2.6) for the splitting  $^{104}\text{Mo}+^{148}\text{Ba}$ . The basis states are given in Table 2.

For the sake of simplicity we dropped the prime upper index for angles. All these curves are centered around  $90^\circ$ , *i.e.*, the fissioning system is not concentrated around the pole-to-pole configuration. On the contrary, for the second resonant state, giving the value on the line 2\*, the angular probability, plotted in Fig. 3 by solid lines, is mainly concentrated in a region of  $\pm 30^\circ$  around the pole-to-pole configuration.

We found out that for the cases 4 and 9 the situation is similar, *i.e.*, the angular probability of the second resonant state belongs mainly to the forward region, in contrast with the first resonance. Moreover, for the splittings 7–10, where the Coulomb barrier is larger, the angular probabilities are more concentrated around the pole-to-pole configuration. This is illustrated in Fig. 4 for the splitting 7 ( $^{106}\text{Mo}+^{146}\text{Ba}$ ).

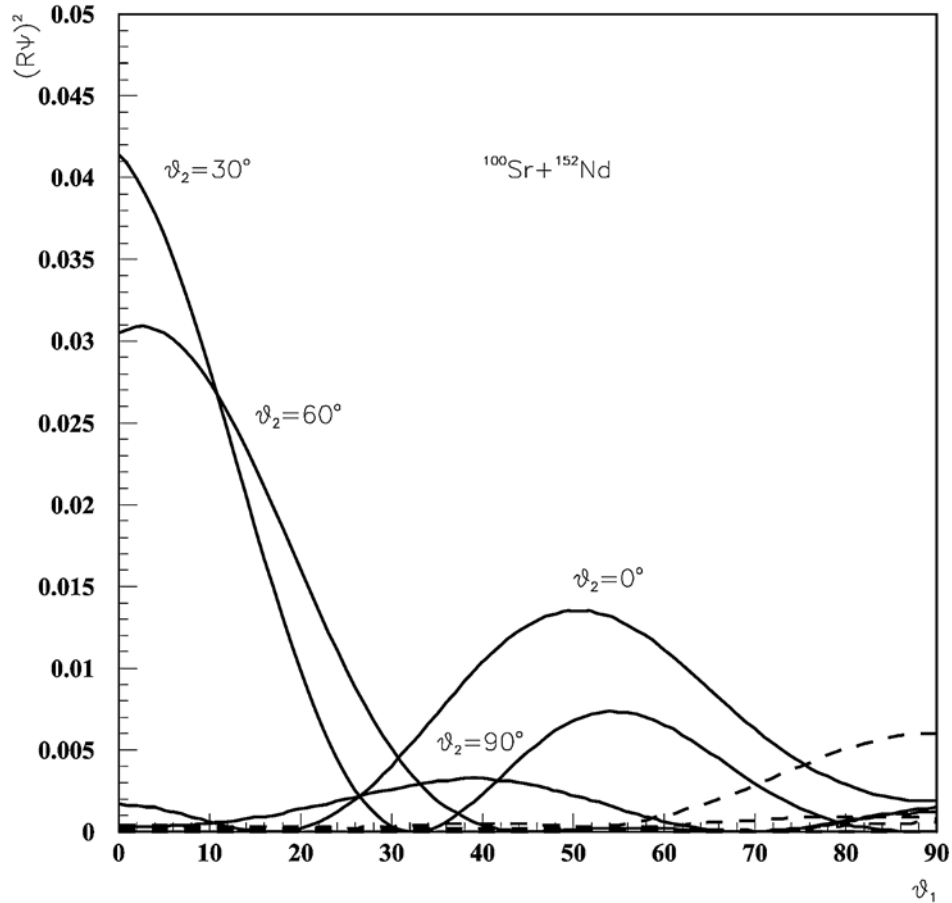


Fig. 3 – The angular part of the wave function *versus* the angle  $\theta_1$  for different angles  $\theta_2$ . By solid lines are given the values corresponding to the second resonant state and by dashes to the first resonance of the system  $^{100}\text{Sr} + ^{152}\text{Nd}$ .

Based on this analysis we selected as fissioning states the lowest possible resonant states which are concentrated around the pole-to-pole configurations. This corresponds to the first resonance, except the cases 2, 4, 9, where we considered the second resonant state ( $2^*$ ,  $4^*$ ,  $9^*$ ).

In our previous Refs. [14, 15] we used in the internal overlapping region a vibrational basis, depending only on “planar” coordinates  $\theta_k$ . This is connected with the strong increasing of the potential along  $\theta_k$ -coordinates, starting from the pole-to-pole configuration. As a result of the integration procedure we obtained in the internal region one predominant vibrational component. In terms of the rotational basis our analysis showed that a vibrational state corresponds to several rotational components with comparable amplitudes. This is indeed our case. In Table 3 we

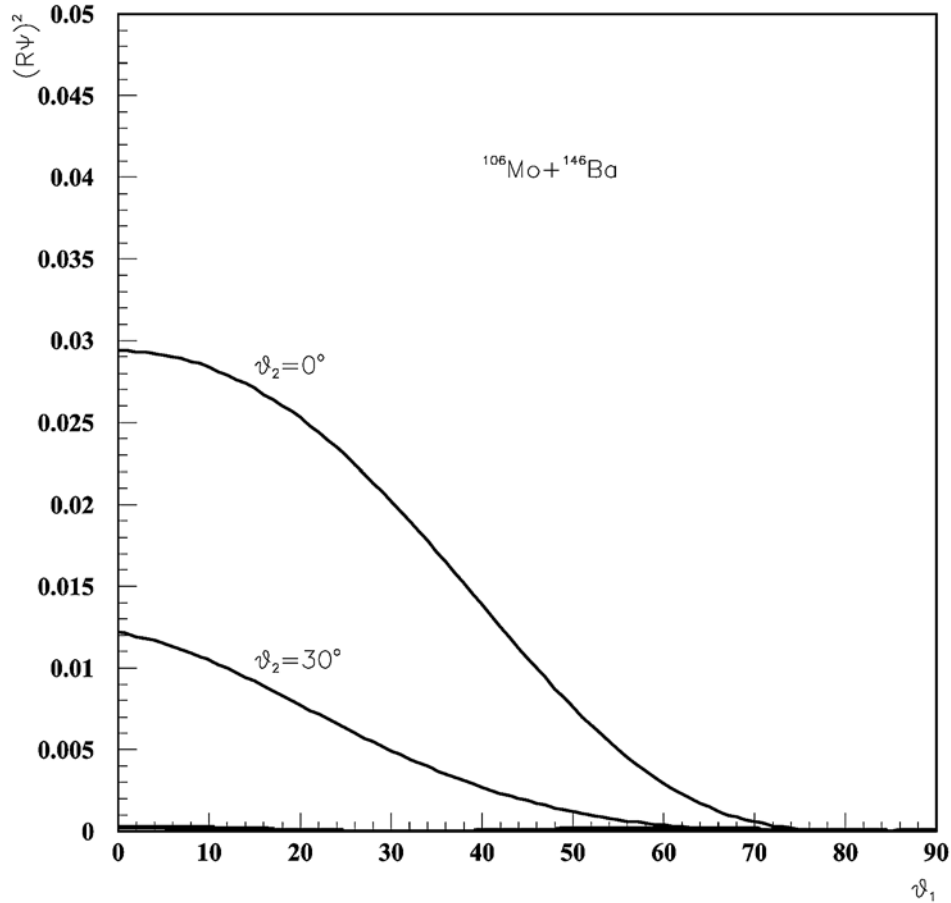


Fig. 4 – The angular part of the wave function *versus* the angle  $\theta_1$  for different angles  $\theta_2$ . The values correspond to the first resonance of the system  $^{106}\text{Mo}+^{146}\text{Ba}$ .

give the mean squared amplitudes, computed according to the following relation

$$\bar{f}_{ll,l_2} = \left[ \int_{R_0}^{R_2} |f_{ll,l_2}(R)|^2 dR \right]^{1/2}. \quad (3.3)$$

One can see that most of amplitudes have comparable values, in agreement with our previous calculation within the internal vibrational basis.

In spite of the fact the amplitudes have different signs, as can be seen from the Fig. 2, we notice that the dependence upon the angular variable  $\theta_1$ ,  $\theta_2$  is mainly concentrated in the forward direction. This feature we can understand from the Table 3. The largest components correspond to the basis elements  $(l, l, 0)$  or  $(l, 0, l)$ . They contribute coherently in the wave function (2.6), giving a diffraction-

Table 3

The averaged amplitudes  $\bar{f}_{ll_1l_2}$  on internal region, defined by Eq. (3.3) for the basis components given in Table 2. The labels in the first column correspond to the splittings given in Table 1

No.	1	2	3	4	5	6	7	8	9	10	11	12	13	14	15
1	.03	.04	.04	.27	.04	.09	.04	.10	.27	.64	.47	.29	.04	.19	.27
2	.47	.13	.07	.50	.48	.28	.07	.08	.11	.17	.25	.18	.08	.13	.17
2*	.12	.05	.07	.32	.15	.11	.07	.09	.34	.54	.39	.38	.06	.18	.28
3	.07	.05	.05	.36	.11	.09	.05	.12	.31	.55	.45	.33	.04	.21	.26
4	.05	.55	.06	.05	.07	.62	.08	.20	.26	.04	.04	.14	.09	.28	.29
4	.05	.09	.08	.33	.05	.17	.09	.09	.30	.54	.43	.37	.05	.15	.32
5	.07	.02	.06	.45	.10	.05	.06	.16	.30	.55	.42	.22	.05	.22	.25
6	.08	.03	.10	.47	.06	.07	.10	.08	.32	.46	.45	.34	.09	.18	.23
7	.25	.27	.14	.29	.36	.30	.14	.21	.23	.22	.30	.42	.15	.19	.22
8	.22	.17	.27	.36	.14	.12	.29	.29	.45	.18	.19	.28	.25	.15	.28
9	.15	.04	.01	.22	.24	.15	.01	.49	.35	.21	.17	.52	.01	.23	.28
9*	.27	.26	.12	.35	.43	.30	.12	.20	.22	.19	.28	.38	.11	.17	.19
10	.26	.26	.14	.41	.35	.30	.15	.23	.24	.22	.22	.37	.13	.19	.20

like pattern around the “planar” pole-to-pole direction for the selected resonant states.

Our method includes also the angles  $\varphi_k$ . We mention here that the angular distribution upon  $\varphi_1 - \varphi_2$  for  $\theta_1 = \theta_2 = 0$  is centered around  $0^\circ$  or  $180^\circ$ . Thus, most of the “torsional” angular distribution is also concentrated around the pole-to-pole configuration.

Let us now analyse the most “controversial” part of our method, namely the internal repulsive core. The procedure to fix the decay energy using an internal repulsive potential was widely used as a phenomenological approach to describe  $\alpha$  and heavy cluster decays. The external barrier, as in our approach, can be estimated on microscopic grounds, using the double folding procedure. From this point of view our analysis is an extension of this approach and the internal repulsive core has only the role in adjusting the energy of some resonant state.

A similar pocket-like interaction was used to describe the so-called quasimolecular resonances in the  $\alpha$  and heavy-ion collisions. In this case the existence of such states is connected with rather large relative angular momenta. Thus, the centrifugal force together with the Pauli principle keeps away the two fragments from the strong nuclear attraction. A real “giant molecule” can exist in our case only for very large relative angular momenta. Our belief is that this possibility really occurs if the initial  $^{252}\text{Cf}$  is in a strongly superdeformed state with a high angular momentum.

Relative small decay widths in our case correspond to rather large half-lives, but they cannot be interpreted in general as the time the fragments live in a

molecular configuration. A small width, as in the usual cluster decay, has the meaning of a small probability for a fission event. This is consistent with the latest experimental findings concerning the gamma-emission from ternary emitted particles in flight [21].

It is already known the important effect of the nuclear deformation on the total decay width in cluster decay processes. Its role increases by increasing the product between the charges of emitted fragments [22]. As was shown in Ref. [12] in the case of cold fission, where the charges of emitted fragments are large, the effect of the hexadecapole deformation on the total widths becomes also important.

Therefore we expect an important role of the quadrupole and hexadecapole deformation parameters on the partial decay widths  $\Gamma_{II_2}$  in Eq. (2.19), describing the double fine structure. To this purpose we investigated the partial yields for each fragment, defined as follows

$$\begin{aligned}\Gamma_I^{(1)} &= \sum_l (\Gamma_{II_2} + \Gamma_{II_4}), \quad I = 2, 4, \\ \Gamma_I^{(2)} &= \sum_l (\Gamma_{I_2I} + \Gamma_{I_4I}),\end{aligned}\tag{3.4}$$

*i.e.*, by excluding the contribution coming from the transition to the gs, as determined in experiments. Here the upper index (1) denotes the first fragment of the splitting in Table 1, while (2) the second one.

In Fig. 5 we studied the role of the quadrupole deformation on the hexadecapole relative yields, defined as

$$\gamma_4^{(k)} = 100 \frac{\Gamma_4^{(k)}}{\Gamma_2^{(k)} + \Gamma_4^{(k)}}, \quad k = 1, 2.\tag{3.5}$$

We analyzed here the splitting 7 ( $^{106}\text{Mo} + ^{146}\text{Ba}$ ) of the Table 1. We considered a fixed quadrupole deformation for the first fragment and changed the deformation of the second fragment around the value in Table 1. One can see first of all that  $\gamma_4^{(1)}$  (solid line) is smaller than  $\gamma_4^{(2)}$  (dashed line). Thus, the experimental situation is reproduced qualitatively. The experimental yields are  $\gamma_4^{(1)} \leq 23$ ,  $\gamma_4^{(2)} = 90[+10, -20]$ .

On the other hand both yields have a significant variation over a relative small interval  $\beta_2^{(2)} \in [0.19, 0.21]$ . Moreover, by changing the deformation of the first fragment from its value  $\beta_2^{(1)} = 0.361$  up to  $\beta_2^{(1)} = 0.330$  the ordering of the two yields becomes inverse. Therefore the relative yields are very sensitive to the quadrupole deformation.

This is also illustrated in Fig. 6, where we plotted the logarithm of total widths in the interval  $\beta_2^{(2)} \in [0.19, 0.21]$  for the same two values of  $\beta^{(1)}$ . An increasing of

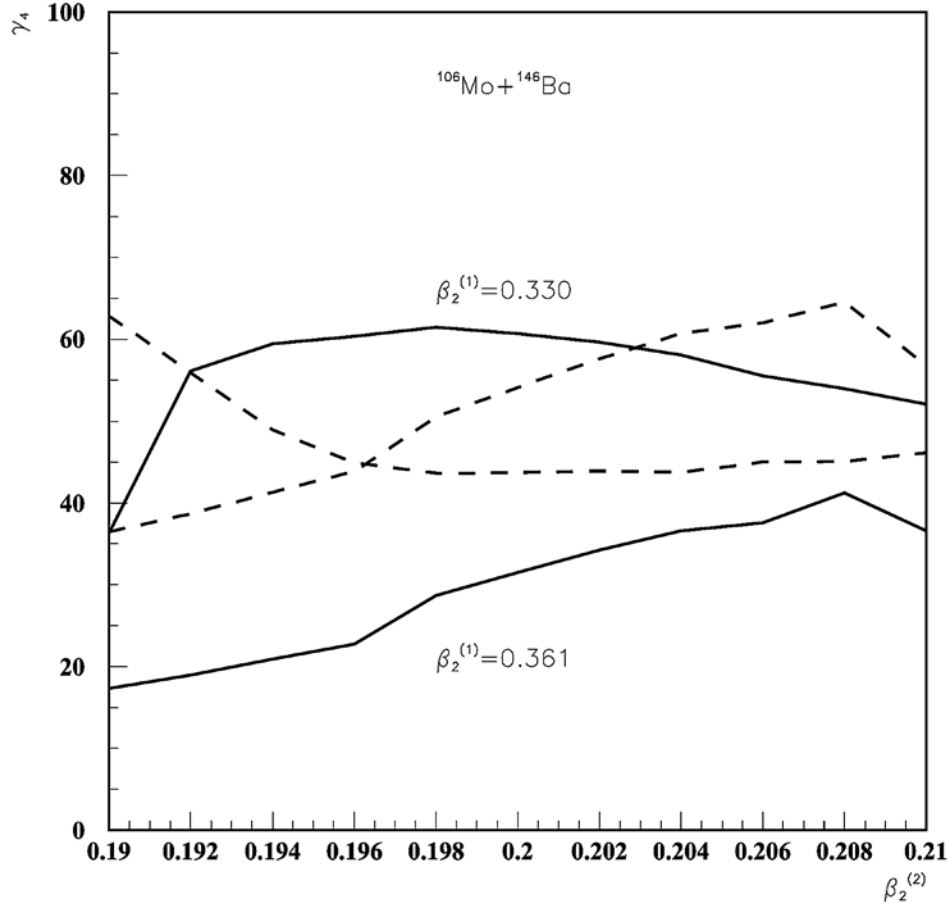


Fig. 5 – The relative hexadecapole yields  $\gamma_4$  defined by Eq. (3.5) versus the quadrupole parameter of the second fragment, for two different quadrupole deformations of the first fragment. The splitting is  $^{106}\text{Mo}+^{146}\text{Ba}$ . By solid lines are given the yields of the  $^{106}\text{Mo}$  and by dashes those of  $^{146}\text{Ba}$ .

the quadrupole deformation by 0.03 increases the total yield by 1.5 orders of magnitude. We mention that this effect is by one order of magnitude more pronounced than for the  $\alpha$ -decay [22].

We investigated in a similar way the role of the hexadecapole deformation. In Fig. 7 we plotted the yields  $\gamma_4^{(1)}$  (solid line) and  $\gamma_4^{(2)}$  (dashed line) versus  $\beta_4^{(2)}$ , in the interval where we found a resonant state. We considered two different values of  $\beta_4^{(1)}$  for the splitting 6 ( $^{104}\text{Mo}+^{148}\text{Ba}$ ) in Table 1. First of all we obtained an inverse ratio of the yields for the two fragments in comparison with the splitting 7 ( $^{106}\text{Mo}+^{146}\text{Ba}$ ). In this case the experimental values are  $\gamma_4^{(1)} = 80 \pm 20$ ,  $\gamma_4^{(2)} \leq 15$ . This is again in a qualitative agreement with the experimental situation.

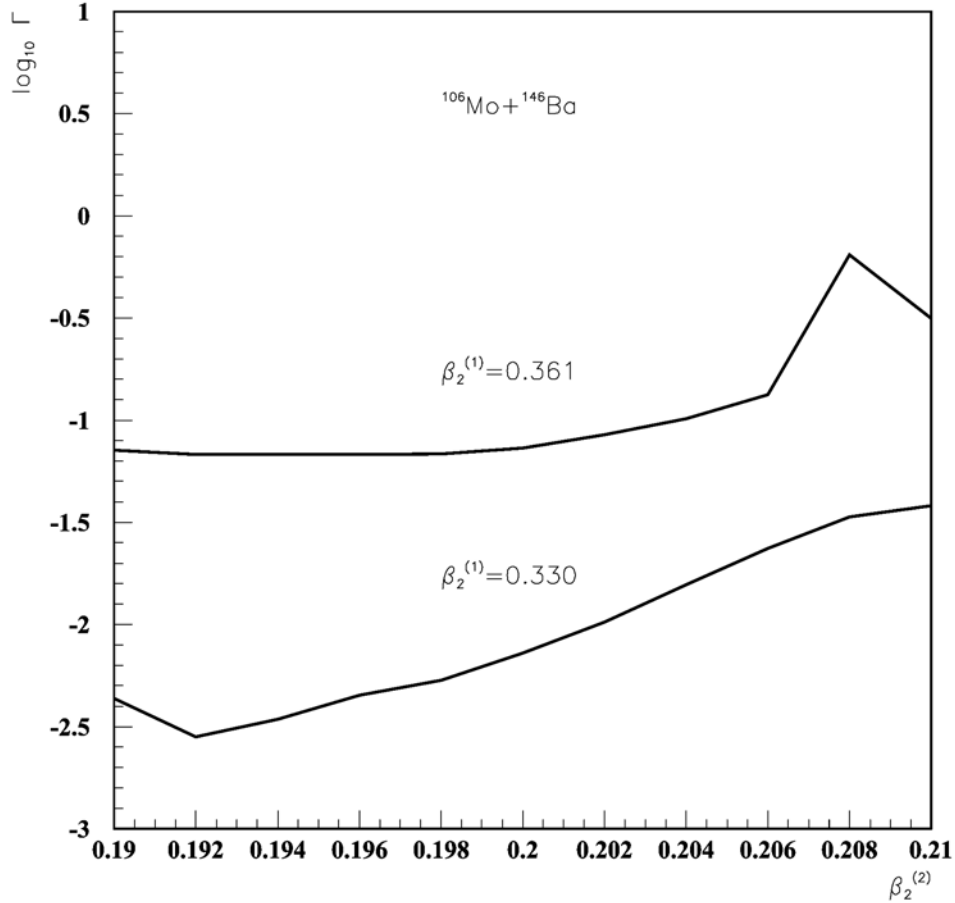


Fig. 6 – The logarithm of the total width *versus* the quadrupole parameter of the second fragment, for two different quadrupole deformations of the first fragment. The splitting is  $^{106}\text{Mo}+^{146}\text{Ba}$ .

Then we can see a rather strong dependence upon this deformation parameter. Moreover, from Fig. 8 one sees that an increasing of the hexadecapole deformation by 0.02 increases the total decay width by almost two orders of magnitude.

A similar situation is depicted in Figs. 9 and 10 for the splitting 7 ( $^{106}\text{Mo}+^{146}\text{Ba}$ ). By taking into account relative large experimental errors we conclude that the experimental situation can be satisfactorily described within our formalism. The differences with respect to experimental values can be also explained by larger than gs deformations of fragments gained in the overlapping region.

Based on this fact we performed some predictions concerning all splittings given in Table 1. Namely, we estimated in Table 4 the relative yields for all possible pairs of angular momenta ( $I_1, I_2$ ), computed as follows

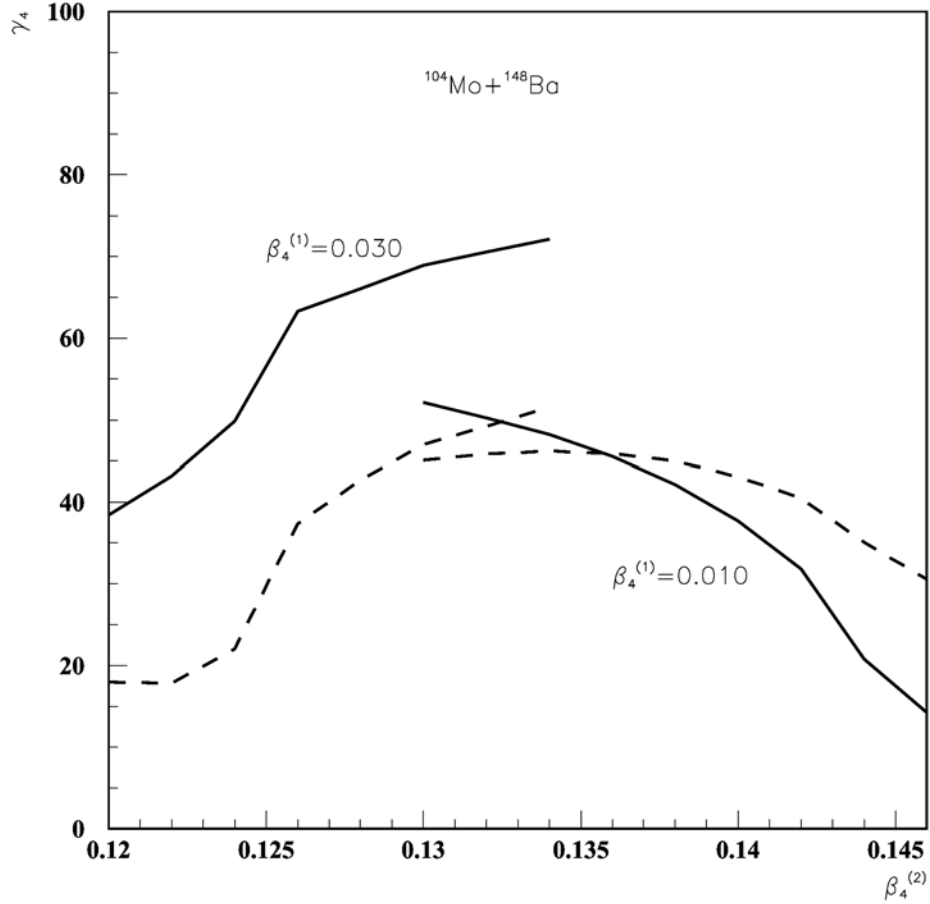


Fig. 7 – The relative hexadecapole yields  $\gamma_4$  versus the hexadecapole parameter of the second fragment, for two different hexadecapole deformations of the first fragment. The splitting is  $^{104}\text{Mo}+^{148}\text{Ba}$ . By solid lines are given the yields of the  $^{104}\text{Mo}$  and by dashes those of  $^{148}\text{Ba}$ . The quadrupole deformations are  $\beta_2^{(1)} = 0.349$ ,  $\beta_2^{(2)} = 0.236$ .

$$\gamma_{I_1 I_2} = 100 \frac{\sum_l \Gamma_{l I_1 I_2}}{\Gamma}. \quad (3.6)$$

Table 4

The relative yields  $\gamma_{I_1 I_2}$ , defined by Eq. (3.6), for the pairs of fragment angular momenta. The labels in the first column correspond to the splittings given in Table 1

No.	(0,0)	(0,2)	(0,4)	(2,0)	(2,2)	(2,4)	(4,0)	(4,2)	(4,4)
1	13.19	13.13	10.80	30.68	4.56	6.50	12.13	6.71	2.30
2	35.33	22.45	4.08	17.90	13.05	2.80	1.02	2.40	0.97

No.	(0,0)	(0,2)	(0,4)	(2,0)	(2,2)	(2,4)	(4,0)	(4,2)	(4,4)
2*	42.80	27.21	5.36	8.14	8.32	2.90	0.67	2.87	1.72
3	11.13	15.66	15.84	0.45	11.90	0.66	20.55	3.73	20.07
4	1.80	1.32	0.12	0.07	75.73	8.28	0.04	10.03	2.60
4*	4.39	6.98	0.07	29.80	9.25	11.09	2.43	30.39	5.60
5	16.72	6.92	1.17	39.18	9.65	0.97	4.74	5.43	15.22
6	3.25	2.14	14.04	2.32	21.61	0.24	39.52	4.43	12.44
7	6.41	10.36	7.89	21.28	15.17	16.20	4.01	7.03	11.65
8	37.45	12.17	6.86	5.38	27.20	5.59	5.05	0.06	0.24
9	2.21	2.78	0.37	23.42	10.26	3.35	7.87	41.37	8.37
9*	5.47	8.19	1.09	1.87	53.52	3.75	2.93	21.32	1.85
10	8.64	11.87	0.19	1.56	36.31	6.48	2.37	5.13	27.46

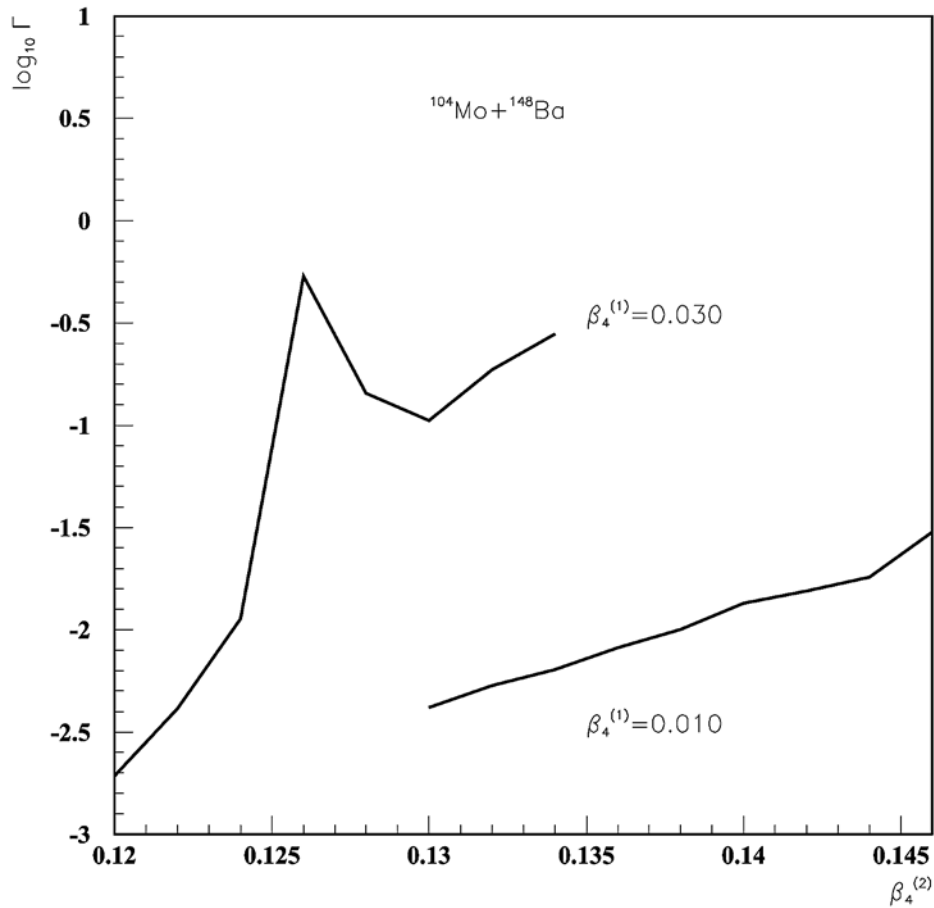


Fig. 8 – The logarithm of the total width *versus* the hexadecapole parameter of the second fragment, for two different hexadecapole deformations of the first fragment. The splitting is  $^{104}\text{Mo}+^{148}\text{Ba}$ .

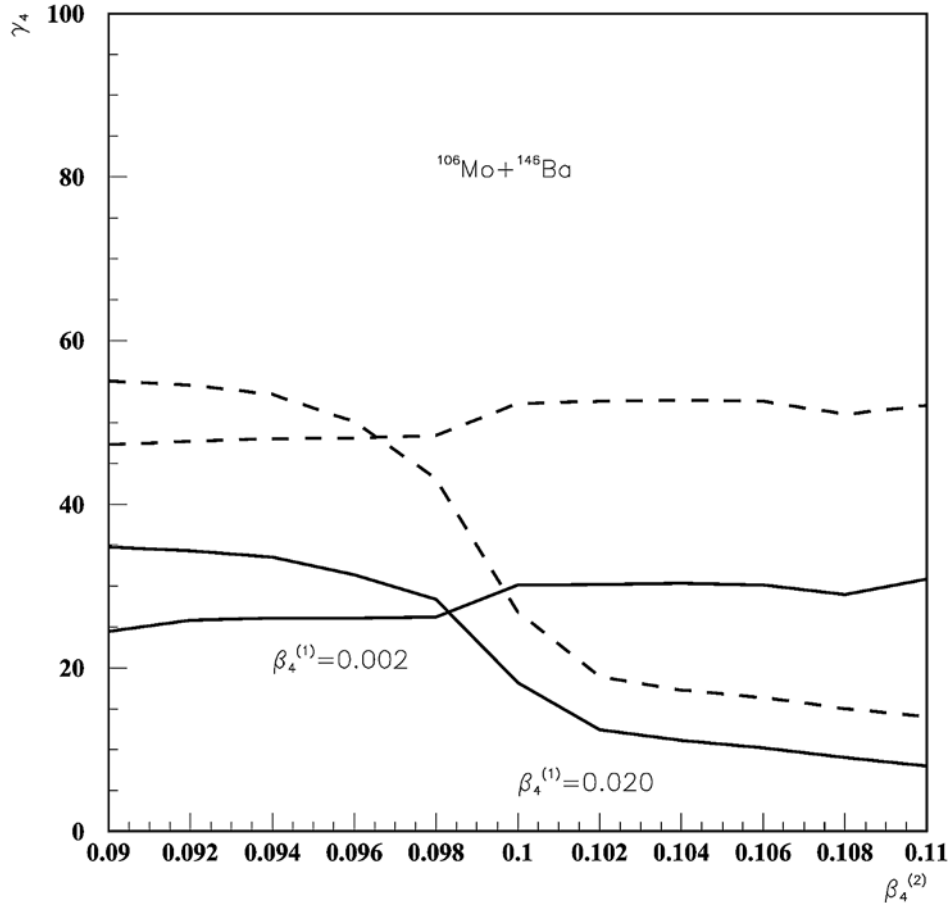


Fig. 9 – The same as in Fig. 7, but for the splitting  $^{106}\text{Mo}+^{146}\text{Ba}$ . The quadrupole deformations are  $\beta_2^{(1)} = 0.361$ ,  $\beta_2^{(2)} = 0.199$ .

We mention first of all that the situation is very different from case to case. On the second hand we can see that in the cases 1, 2, 2\*, 3, 5, 7 the gs-gs combination is larger than 10%. On the third hand the relative yields in the pair cases (2, 2\*); (4, 4\*) and (9, 9\*) are significantly different. Therefore a proper experimental setup, measuring the above relative yields, would be some kind of “microscope” able to “see” into the relative wave-function components inside the potential barrier. The situation is similar for proton or  $\alpha$ -decay fine structure, revealing the details of the internal structure. Here the correlation with the nuclear structure details is enhanced due to the following three factors:

- 1) the double fine structure of the measured widths,
- 2) large fragment charges,
- 3) a relative low Coulomb barrier.

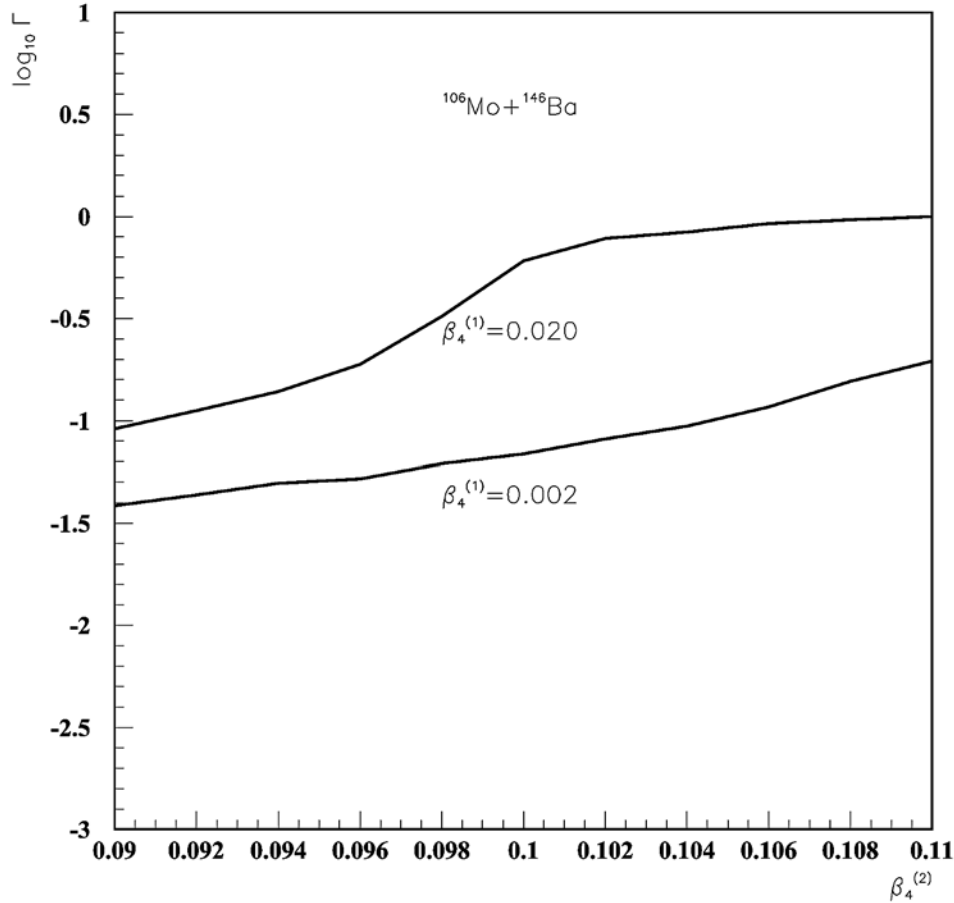


Fig. 10 – The same as in Fig. 8, but for the splitting  $^{106}\text{Mo} + ^{146}\text{Ba}$ .

#### 4. CONCLUSIONS

In this paper we improved and simplified our previous formalism to compute the decay probabilities to final rotational states from the fissioning nucleus  $^{252}\text{Cf}$ . To this purpose we used a common rotational basis in order to describe resonant states within the stationary scattering theory.

We estimated the mutual interaction of the two fragments by using the double folding procedure with M3Y two-body plus Coulomb forces. We reproduced the experimental position of the resonant state by an internal repulsive delta-force core. By changing the repulsive strength it is possible to obtain different resonant states inside the resulting pocket-like potential.

We showed that some resonant states have an angular distribution of the probability which is mainly concentrated around the pole-to-pole configuration both in the “planar” and “torsional” degrees of freedom. We choosed them as the best candidates describing cold fission process.

We analyzed the role played by quadrupole and hexadecapole deformation parameters. We showed that the relative yields are very sensitive to these parameters. The total decay width increases by one order of magnitude if one increases one of the deformation parameters by 0.02.

We were able to describe qualitatively the experimental situation for two measured splittings, assuming the deformation parameters given by independent calculations. The differences beyond experimental errors can be explained by larger deformations of fragments in the overlapping region. We also predicted relative yields/pairs of fragment spins for ten most intense splittings of  $^{252}\text{Cf}$ .

Thus, the cold fission process involving transitions to low-lying states is an useful tool to investigate nuclear structure details. We hope that the conclusions of this paper will encourage experimentalists to perform an extensive analysis concerning the double fine structure of fission products.

## REFERENCES

1. G. M. Ter-Akopian, *et al.*, Phys. Rev. Lett., **73** (1994) 1477.
2. A. Săndulescu, A. Florescu, F. Carstoiu, W. Greiner, J. H. Hamilton, A. V. Ramayya, and B. R. S. Babu, Phys. Rev. C, **54** (1996) 258.
3. A. V. Ramaya, J. H. Hamilton, J. K. Hwang, and G. M. Ter-Akopian, *Heavy Elements and Related New Phenomena*, Vol I, Eds. R. K. Gupta and W. Greiner (World Scientific, Singapore, 1999) p. 477.
4. A. V. Ramayya *et al.*, in Proceedings of the Second International Conference “Fission and Properties of Neutron-Rich Nuclei”, Eds. J. H. Hamilton, W. R. Philips, and H. K. Carter, St. Andrews, Scotland, June 28–July 3, 1999, (World Scientific, Singapore, 1999) p. 246.
5. J. H. Hamilton, *et al.*, in Proceedings of the Symposium on “Fundamental Issues in Elementary Matter” Ed. W. Greiner, Bad Honnef, Germany, September 25–29, 2000 (Ep Systema, Debrecen, Hungary, 2000) p. 151.
6. S.-C. Wu *et al.*, Phys. Rev., C **62**(2000) 041601.
7. A. V. Ramayya *et al.*, Progr. Part. Nucl. Phys., **46** (2001) 221.
8. M. Jandel *et al.*, J. Phys. (London) G **28** (2002) 2893.
9. J. H. Hamilton *et al.*, Yad. Fiz., **65** (2002) 677; Phys. At. Nucl., **65** (2002) 695.
10. A. Săndulescu and W. Greiner, J. Physics (London) G **3** (1977) L189.
11. A. Săndulescu and W. Greiner, Rep. Prog. Phys., **55** (1992) 1423.
12. A. Săndulescu, Ş. Mişicu, F. Carstoiu, A. Florescu, and W. Greiner, Phys. Rev., C **58** (1998) 2321.
13. J. O. Rasmussen *et al.*, in Proceedings of the third International Conference “Dynamical Aspects of Nuclear Fission”, Eds. J. Kliman and B. I. Pustynnik Častá-Papiernička, Slovak Republic, August 30–Sept 4, 1996, (JINR, Dubna, 1996) p. 289.
14. D. S. Delion, A. Sandulescu, S. Misicu, F. Carstoiu, and W. Greiner, Phys. Rev., C **64** (2001) 041303.
15. D. S. Delion, A. Sandulescu, S. Misicu, F. Carstoiu, and W. Greiner, J. Phys. (London) G **28** (2002) 289.

16. D. S. Delion, A. Sandulescu, and W. Greiner, *Phys. Rev., C* **68** (2003) 041303(R).
17. Ş. Mişicu, A. Săndulescu, and W. Greiner, *Phys. Rev., C* **64** (2001) 044610.
18. F. Carstoiu and R. J. Lombard, *Ann. Phys. (N.Y.)* **217** (1992) 279.
19. G. Bertsch, J. Borysowicz, H. McManus, and W. G. Love, *Nucl. Phys. A* **284** (1977) 399.
20. P. Möller, J. R. Nix, W. D. Myers, and W. J. Swyatecki, *At. Data Nucl. Data Tables* **59** (1995) 185.
21. J. K. Hwang *et al.*, Proceedings of the “Symposium on Nuclear Clusters”, Eds. R. Jolos and W. Scheid, Rauschholzhausen, Germany, August 5–9, 2002, (Ep Systema, Debrecen, Hungary, 2003) p. 257.
22. D. S. Delion, A. Insolia, and R.J. Liotta, *Phys. Rev. Lett.*, **78** (1997) 4549.